Research Article

A combined theoretical and experimental study on the structure, vibrational, and electronic properties of antiparkinsonian drug safinamide

Ana Estela Ledesma[1] · **César Atilio Nazareno Catalán**[2] · **Silvia Antonia Brandán**[3]

Received: 20 July 2020 / Accepted: 10 October 2020

Abstract
In this work, structural, electronic, topological, and electronic and vibrational spectra of antiepileptic and antiparkinsonian drug safinamide (two enantiomers and their mesylate salt) were investigated with the DFT/TD-DFT methodology in gas phase and PCM solvent model. The absorbance maximum of safinamide was found at 227 nm, and the computed maximum transition occurred at 226 nm, which was assigned to $\pi \rightarrow \pi^*$ transitions due to the chromophores C=C, C=O and C=N bonds. Electrostatic potential maps of all studied molecules revealed that the C=O group of (*S*)-enantiomer was more nucleophilic than the remaining molecules. Topological analysis suggested that an N–H intramolecular hydrogen bond especially in solution, and the NBO study showed a clear instability and strong ionic character of the salt. The lower electrophilicity and nucleophilicity indexes for the (*S*)-enantiomer than for the (*R*)-enantiomer, the higher reactivity it shows. At the same time, it shows higher activity as inhibitor of monoamine oxidase B. The force fields and the complete assignment of the 117 vibration normal modes of the enantiomers and 144 vibration normal modes of the mesylate salt are reported. The predicted infrared, Raman, ^{1}H-NMR, UV–visible, and ECD spectra were in reasonable agreement with the corresponding experimental ones. In addition, the interaction with monoamine oxidase was evaluated. This study provides a structural, vibrational, and electronic characterization of the drug through theoretical insights that will contribute to further research of the biological interaction mechanism.

Keywords (*S*)-safinamide · (*R*)-safinamide · (*S*)-safinamide mesylate · Vibrational spectra · Molecular structure · DFT calculations

1 Introduction

Safinamide is an oral α-aminoamide derivative with anticonvulsant and antiparkinsonian activity used for the treatment of Parkinson's disease (PD) [1–4]. It has both dopaminergic and non-dopaminergic (glutamatergic) properties; the former, due to its selective and reversible monoamine oxidase B (MAO-B) inhibition and dopamine reuptake inhibition and the latter, via blocking of voltage-sensitive sodium and calcium channels, as well

Electronic supplementary material The online version of this article (https://doi.org/10.1007/s42452-020-03661-7) contains supplementary material, which is available to authorized users.

✉ Ana Estela Ledesma, anael@unse.edu.ar | [1]Departamento Académico de Química, Facultad de Ciencias Exactas y Tecnologías, Universidad Nacional de Santiago del Estero, Centro de Investigaciones en Biofísica Aplicada y Alimentos (CIBAAL-UNSE- CONICET), Av. Belgrano Sur 1912, 4200 Santiago del Estero, Argentina. [2]Instituto de Química Orgánica, Facultad de Bioquímica, Química y Farmacia, Universidad Nacional de Tucumán, Ayacucho 471, T4000INI San Miguel de Tucumán, Tucumán, Argentina. [3]Cátedra de Química General, Instituto de Química Inorgánica, Facultad de Bioquímica. Química y Farmacia, Universidad Nacional de Tucumán, Ayacucho 471, 4000 San Miguel de Tucumán, Tucumán, Argentina.

Published online: 26 October 2020

as glutamate release inhibition [5]. Animal models demonstrated that safinamide has neuroprotective and neurorescuing properties that may be attributed to its non-dopaminergic activity [6], but there are no data on the neuroprotective effects of safinamide in humans.

The chemical name of safinamide is (+)-(*S*)-2-[[p-[(m-fluorobenzyl)oxy]benzyl]amino]propionamide monomethanesulfonate; it is a white to off-white, non-hygroscopic crystalline solid, water soluble, and shows pH dependent solubility in aqueous buffers [7]. The most thermodynamically stable form, the anhydrous form, was selected for commercialisation. Two orthorhombic conformational forms were reported for safinamide, which differ only in the orientation of 3-fluorobenzyloxy and propanamide groups [8]. They have a difference of up to 4.7 degrees in the exocyclic angle involving the C1 atom of 3-fluorobenzyloxy ring, and N–H–O hydrogen bonds are observed in both structures, since N–H–F hydrogen bonding is present in (I) form, while N–H–N hydrogen bonding is present in (II) form. The synthesis of safinamide from (*S*)-alaninamide as a single enantiomer can be accompanied by traces of undesired (*R*)-enantiomer that can be present as an impurity and would show signs of toxicity at lower doses than those of the *S*-enantiomers [9]. In the last years, using HPLC methods, it has been possible to identify and characterize four process-related impurities in the manufacture of bulk drug and five degradation products under oxidative conditions to the bulk safinamide mesylate [10]. A previous report indicated possible enantioselective interactions at the enzyme binding site and hence, the (*S*)-enantiomer of safinamide exhibited a significantly higher affinity and selectivity for MAO-B (IC50 = 0.098 μM and SI = 5918, respectively) than the corresponding (*R*)-enantiomer (IC50 = 0.45 μM and SI = 93) [11]. In this context, the knowledge and structural characterization of the (*S*)- and (*R*)-enantiomer of safinamide are relevant to understand the stereochemical factors involved in their biological activity. Nowadays, there is no information about the characteristic properties of both enantiomers of safinamide and the (*S*)-safinamide mesylate salt. Thus, in this study we explore the electronic structure, structural and vibrational features of those molecules, and also compare the effects of mesylate group on the studied properties, because these properties have not been reported so far. The experimental measurements are also compared with those of density functional theory (DFT) calculations, where the stabilization in PCM model, frontier orbitals (HOMO, LUMO), and gap (Eg) energies, IR and Raman intensity, reactivities, NMR spectrum, and dipole moments are calculated at that level of theory. Using time-dependent (TD)-DFT technique, the predicted absorption of excited states and the optical energy gap are calculated for all species, and compared with ultraviolet visible (UV–Vis) and electronic circular dichroism (ECD) spectra in aqueous solution. Finally, topological properties are discussed in detail.

2 Experimental methods

The mesylate salt of the (*S*)-(+)-enantiomer of safinamide, hereafter referred to a SMS, was purchased from Sigma-Aldrich. FTIR spectra in solid phase were recorded in a Thermo Nicolet 6700 FTIR equipped with a DTGS KBr detector and KBr beam splitter. A multiple bounce ATR smart accessory was used for recording spectra with a resolution of 4 cm^{-1} and 128 scans. The FTIR spectra were processed using OPUS version 7.0 software. The Raman spectrum of SMS in the solid phase was recorded between 3500 and 50 cm^{-1} at room temperature with a Thermo Scientific, DXR Raman Microscope (Thermo Fisher Scientific) equipped with a laser (excitation line of 1532 nm, 10 mW of laser power). The Raman spectrum was recorded with a resolution of 4 cm^{-1} and 300 scans.

The UV absorption spectrum of a 190 μM aqueous solution of SMS was recorded on a Shimadzu UV–Vis 1800 spectrophotometer in the spectral region of 200–600 nm. A quartz cuvette with 1 cm path length was used, and all the solutions were prepared in tri-distilled water.

The electronic circular dichroism spectrum of the same aqueous solution was recorded in a 1 mm path length quartz cuvette using a Jasco J-815 CD spectrometer.

2.1 Computational details

The initial structures of the (*S*)- and (*R*)-enantiomers of safinamide and of SMS were initially built with the GaussView program [12], taking into account the experimental structures reported by Ravikumar [8]. All calculations were performed using the hybrid B3LYP/6-31G* method with the Gaussian 16 program [13]. The influence of the solvent was studied by using the self-consistent reaction field (SCRF) method together with the integral equation formalism variant polarised continuum model (IEFPCM) at the same level of theory [14], and the predicted solvation energies involved in the dissolution process were computed with the solvation model (PCM/SMD) [15]. Structural properties of the three species were investigated by using the natural population atomic (NPA) charges, bond orders (Wiberg index), molecular electrostatic potentials (MEP), stabilization energies, and topological properties were computed in both media (gas phase and aqueous solution) with the NBO 6.0 [16] and AIM2000 programs [17]. Here, the Merz-Kollman (MK) charges were also considered, while the reactivities were predicted by using the frontier molecular orbitals and some descriptors [18]. On the other hand, the

SQMFF methodology [19] and the MOLVIB program [20] were used to compute the complete assignments for the two enantiomers and for SMS. The UV–Vis and ECD spectra in aqueous solution were also predicted using time-dependent density functional theory (TD-DFT).

3 Docking calculations

The binding site for both enantiomers and SMS in the enzyme cavity was characterized by molecular docking, using AutoDock 4.2 tool [21] with a semiempirical free-energy force. The crystal structure of MAO-B was obtained from Protein Data Bank (available online: http://www.rcsb.org/pdb, PDB ID: 2V5Z), and the docking calculation was performed using Lamarckian genetic algorithm (LGA). To evaluate the atomic interactions in the binding sites, a grid point of 80 × 80 × 80 was built, and 0.375 Å grid spacing was considered. Safinamide and SMS were treated as rigid docking, and from the best conformation, the free energy of ligand binding and the inhibition constant were estimated.

The best cluster obtained from docking studies of (*S*)-enantiomer-MAO-B complex was used to estimate the donor–acceptor interactions in the active site of the enzyme-inhibitor complex. NBO analysis was performed using the ONIOM method, where the ligand was assumed as the QM region and the residues in the active site as the MM region. DFT method employing B3LYP/6-31G* basis set was used for the high-level part of system (ligand), and AMBER method was used for the remaining part of system.

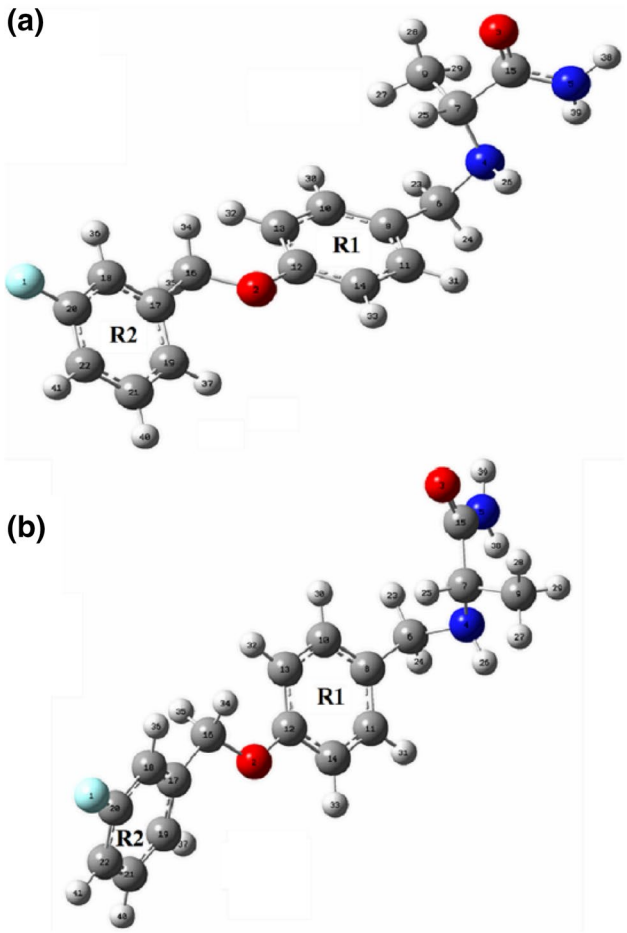

Fig. 1 Molecular theoretical structures of both enantiomers of safinamide: **a** (*R*)-safinamide and **b** (*S*)-safinamide and atom numbering. The identification of the aromatic rings is also included

4 Results and discussion

4.1 Geometry and energy stabilization

The optimized structures of the (*S*)- and (*R*)-enantiomers are shown in Fig. 1, while the structure corresponding to SMS is presented in Fig. 2. The structural properties including solvation energies for the (*R*)- and (*S*)-enantiomers of safinamide and for SMS in gas phase and aqueous solution are listed in Table 1. The (*S*)-form is the most stable enantiomer in both media, its population being ca. 98% in the gas phase with an energy difference of 9.44 kJ/mol with the (*R*)-enantiomer. A decrease in volume and population can be observed for the (*S*)-enantiomer in aqueous solution, which could be attributed to the rearrangement of electric charges as a result of interactions with solvent molecules. The high volume variation for the (*R*)-enantiomer probably indicates a destabilization of this species, as supported by its higher uncorrected solvation energy in relation to the (*S*)-enantiomer. The significant increase in the dipole moment values for both species from the gas phase to aqueous solution would be attributed to their highly hydrated structures in solution. Calculated molecular geometry parameters of all structures in gas phase and water are presented in Table S1 in Supporting Information and they are compared with the experimental X-ray crystallographic data [8]. The differences between calculated and experimental values are between 0.032 and 0.023 Å for bond lengths in both media, while variations in bond angles are between 2.6° and 0.9°.

The main differences between the (*S*)- and (*R*)-enantiomer are in the N4–C7 and C7–C15 bonds of the chiral centre, where the (*S*)-enantiomer shows lower values in solution. The dihedral angles for the (*S*)-(I) form in both media show lower deviation from experimental data, and the greater differences observed in the dihedral angles for the (*R*)-enantiomer clearly indicates that its presence is strongly disfavoured.

The slight volume compression in solution observed for SMS and the higher corrected solvation energy value

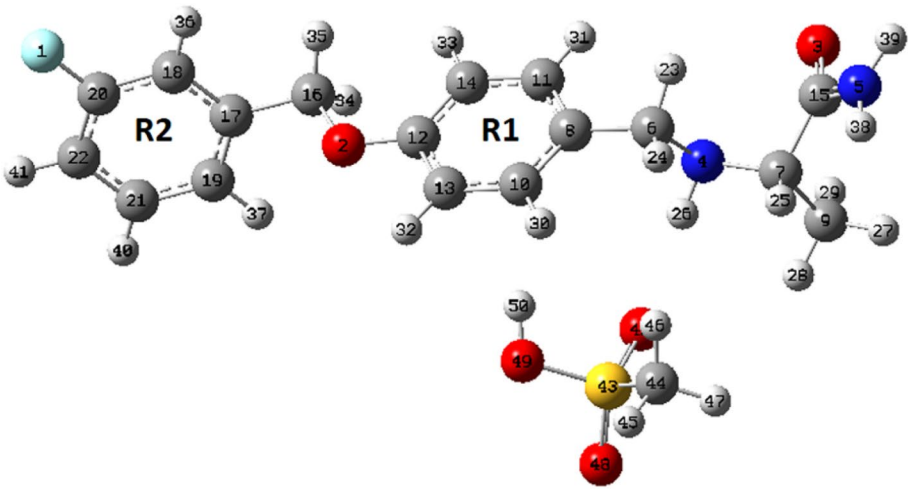

Fig. 2 Molecular theoretical structure of SMS and atom numbering. The identification of the aromatic rings is also included

Table 1 Calculated total (*E*) and relative energies (Δ*E*), dipole moments, volume variation, and solvation energy for the two enantiomers of safinamide in gas and aqueous solution phases

B3LYP/6-31G*					
GAS					
Species	E (Hartrees)	μ (D)	V (Å^3)	ΔE (kJ/mol)	Population%
S-(I)	− 1019.0415	3.74	333.6	0.00	97.85
R	− 1019.0379	4.11	336.2	9.44	2.15
SMS	− 1683.3535	5.38	406.2		
PCM					
S	− 1019.0624	5.65	332.4	0.00	94.61
R	− 1019.0597	6.35	330.5	7.08	5.39
SMS	− 1683.3925	9.20	403.6		
Solvation energy (kJ/mol)					
	$\Delta G_u^{\#}$	ΔG_{ne}	ΔG_c	ΔV (Å^3)	
S-(I)	− 54.82	30.43	− 85.25	− 1.2	
R	− 57.18	30.68	− 87.86	− 5.7	
SMS	− 104.4	32.2	− 134.6	− 2.6	

$\Delta G_u^{\#}$ = uncorrected solvation energy: defined as the difference between the total energies in aqueous solution and the values in gas phase

ΔG_{ne} = total non-electrostatic terms: due to cavitation, dispersion, and repulsion energies

ΔG_c = corrected solvation energies: defined as the difference between the uncorrected and non-electrostatic solvation energies

(− 134.52 kJ/mol) could be attributed to hydration with water molecules. The high value of corrected solvation energy in water reveals that the thermodynamic factor is responsible for the stability of the mesylate salt in that medium, corresponding with the reported enantioselective synthesis for safinamide and derivatives [9]. Slight differences in the values for bond angles and bond distances are predicted for gas phase and aqueous medium, in comparison to the two experimental forms of (*S*)-safinamide, with deviation values around 0.032 and 0.024 Å for bond distances and variations in the bond angles between 2.6° and 1.3°, respectively. The obtained dihedral angles for the salt in gas phase has the highest deviation from experimental data; those differences are markedly reduced from 94.2° and 143.5° to 48° and 10° in water.

4.2 Charges and MEP studies

In order to compare the Merz-Kollman and natural population atomic charges, only the common parts of the (*S*)- and (*R*)-enantiomers of safinamide and SMS were considered (Table S2 of Supporting Information). The main differences

were predicted for the alanineamide group atoms. A detailed analysis of charges on the C atoms showed that the highest negative values were predicted for the C9 atom corresponding to the CH_3 group attached to the chiral carbon atom C7, while the most positive charges were observed on the C15 atom for SMS. This last result agrees with the shorter bond length values observed for the O3=C15 bond of the carbonyl group. In relation to the N atoms, the highest NPA and MK charges were observed on the N5 atoms, as expected, because these atoms clearly reveal the ionic characteristics of mesylate group. These results show the importance of the charge distribution on the structures in both media and besides they support the nature of the different bonds. The NPA charges predicted on the C6 and C7 atoms of alanineamide group of all species were negative, while their predicted MK charges were positive. The calculated bond orders (BO), expressed as Wiberg bond index for O2 and O3 atoms of SMS in gas phase, had lower values than the (*S*)-enantiomer, and both atoms increased their values in solution, indicating different characteristics of these bonds in the salt, especially in aqueous solution (Table S3), which suggests that those atoms were solvated by water molecules. A similar behaviour showed that the N4 and N5 atoms belonging to the salt whole Wiberg bond index increased as a result of hydration.

A highly nucleophilic centre can be seen in the two enantiomers, on the C=O group, and electrophilic centres on the H atoms belonging to the NH_2 group, and in mesylate salt the nucleophilic sites significantly increased due to the O atoms belonging to the $HO–SO_3–CH_3$ group. Thus, SMS showed strong red colours on the O3 and N4 atoms and slight red colours on the O atoms belonging to the $HO–SO_3–CH_3$ group, while light blue colours were observed on the NH_2 and CH_3 groups belonging to the alanineamide moiety, as shown in Fig. 3. The analysis of molecular electrostatic potential values of all molecules in both media is presented in Table S3.

4.3 Electronic delocalizations analysis

In order to evaluate the intramolecular interactions, stabilities and delocalization energies for both enantiomers and SMS, those three elements were analysed as well as the topological properties of electron density, provided details of atomic, molecular, and chemical bonding. The differences in donor–acceptor energy in gas phase and aqueous solution are given in Table 2. The main contribution to calculated transitions are of inter-ring $\pi \rightarrow \pi^*$ character, which explains their strong delocalization energies between the two rings. In solution, (*S*)-enantiomer and the salt showed strong contribution to delocalization energy from lone pair orbitals to antibonding ($LP \rightarrow \pi^*$) transitions and a decrease in $LP \rightarrow \sigma^*$ transitions. The results showed that the main contribution to stabilization energy was between antibonding π^* orbitals of the R1 ring, and from LP (O) or (N) orbital to antibonding $\sigma^*C–N$ and $\sigma^*C–O$ orbitals, in agreement with recent reports in gas phase [22]. The total energies evidence a clear instability of the mesylate salt in both media, as compared with the two enantiomeric forms of the free amine due to the strong ionic characteristics of the alaninamide group in the mesylate salt.

These results would indicate the high stability of the salt in solution and, probably, its high activity as inhibitor

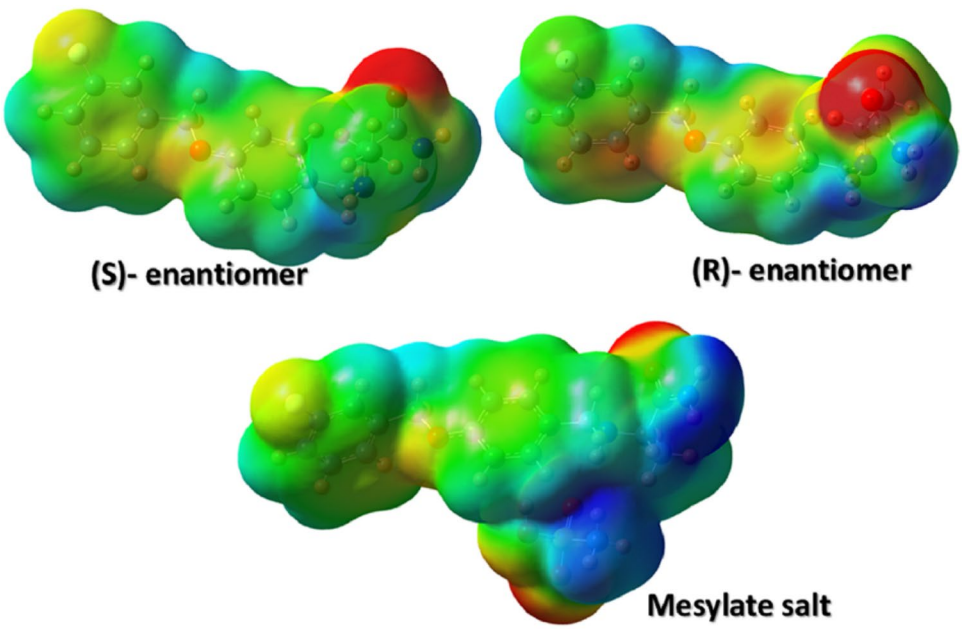

Fig. 3 Calculated electrostatic potential surfaces on the molecular surfaces of (*S*)- and (*R*)-enantiomers of safinamide and (*S*)-safinamide mesylate salt (SMS) in gas phase. Colour ranges, in au: from red – 0.070 to blue + 0.070. B3LYP functional and 6-31G* basis set. Isodensity value of 0.005

Table 2 Main delocalization energy (in kJ/mol) for the two enantiomers of safinamide and SMS in gas phase and in aqueous solution at B3LYP/6-31G* level of theory

Delocalization	*S*-(I)		*R*		SMS	
	Gas	PCM	Gas	PCM	Gas	PCM
$\pi C8–C10 \rightarrow \pi^*C11–C14$	90.16	89.66	88.49	90.16	101.70	97.43
$\pi C8–C10 \rightarrow \pi^*C12–C13$	75.15	74.44	74.57	75.16	80.13	77.12
$\pi C11–C14 \rightarrow \pi^*C8–C10$	73.07	73.40	73.65	73.07	68.72	69.97
$\pi C11–C14 \rightarrow \pi^*C12–C13$	87.86	87.48	87.69	87.86	83.81	82.68
$\pi C12–C13 \rightarrow \pi^*C8–C10$	88.95	86.66	88.36	88.95	88.70	90.87
$\pi C12–C13 \rightarrow \pi^*C11–C14$	71.10	71.39	70.68	71.10	76.16	76.08
$\pi C17–C18 \rightarrow \pi^*C19–C21$	74.36	74.78	74.36	74.36	74.49	76.54
$\pi C17–C18 \rightarrow \pi^*C20–C22$	97.39	97.27	97.10	97.39	97.94	96.14
$\pi C19–C21 \rightarrow \pi^*C17–C18$	94.59	93.13	94.38	93.21	94.76	92.38
$\pi C19–C21 \rightarrow \pi^*C20–C22$	79.13	78.71	79.08	79.13	79.13	80.05
$\pi C20–C22 \rightarrow \pi^*C17–C18$	76.95	77.04	76.99	76.95	76.83	78.75
$\pi C20–C22 \rightarrow \pi^*C19–C21$	86.36	85.27	86.19	86.36	86.57	84.35
$\boldsymbol{\Delta ET_{\pi \rightarrow \pi^*}}$	995.07	989.23	991.54	993.7	1008.9	1002.4
$LP(3)F1 \rightarrow \pi^*C20–C22$	84.43	82.51	84.47	84.43	84.31	82.39
$LP(2)O2 \rightarrow \pi^*C12–C13$	125.10	122.43	125.90	125.11	124.06	126.44
$LP(1)N5 \rightarrow \pi^*O3–C15$	251.46	219.07	238.34	251.47	240.01	261.46
$\boldsymbol{\Delta ET_{LP \rightarrow \pi^*}}$	460.99	424.01	448.71	461.01	448.4	470.3
$LP(2)O3 \rightarrow \sigma^*N5–C15$	106.50	96.51	107.05	106.50	108.64	97.85
$LP(2)O3 \rightarrow \sigma^*C7–C15$	87.99	80.50	87.86	87.99	92.67	85.73
$\boldsymbol{\Delta ET_{LP \rightarrow \sigma^*}}$	194.49	177.01	194.91	194.49	201.3	183.6
$\pi^*C12–C13 \rightarrow \pi^*C8–C10$	922.77	968.50	913.66	922.77	673.48	563.67
$\pi^*C14–C11 \rightarrow \pi^*C8–C10$	–	–	–	–	500.68	774.43
$\boldsymbol{\Delta ET_{\pi^* \rightarrow \pi^*}}$	922.77	968.50	913.66	922.77	1174.16	1338.1
$\boldsymbol{\Delta E_{Total}}$	**2573.32**	**2558.75**	**2548.82**	**2571.97**	**2832.8**	**2994.4**

Total energies expressed in bold letters

of MAO-B [23, 24], due to the extended conformation with the 3-fluorobenzyloxy moiety and the primary amide group oriented towards the flavin cofactor [23]. Notably, diverse electronic and hydrophobic properties of mesylate salt due to the fluorobenzyloxy group may suggest an important steric effect as the most likely cause of the observed increase in affinity [24].

Topological analysis clearly showed the contribution of some intermolecular contacts present in the molecules. Thus a strong N4–H38 hydrogen bonding interaction for two enantiomers in both media, and for the (*R*)-enantiomer in the gas phase, and an additional bond critical point (BCP), namely H27–H30, were predicted, so two new ring critical points (RCPs) were calculated (RCP3 and RCP4), and can be seen in Table S4. These results could justify the greater stability of (*R*) against (*S*), in gas phase, while in aqueous solution the similar values in the parameters of RCP1 and RCP2 could support the presence of both forms in solution.

In relation to SMS, the electron density, the Laplacian and electron localization function in gas phase revealed the formation of two (C–H and O–H) hydrogen bond interactions as well as an O–C interaction, as clearly shown in Fig. 4 and Table S5. In aqueous solution, additional donor and acceptor interactions were predicted, thus five different bond interactions could be observed, namely C44–H28, H50–C10, H26–O42, H30–H46, and H46–H26 with lower electron density values. Therefore, the stability of salt in gas phase (approximating to solid phase behaviour) is different than in aqueous solution.

4.4 Electronic and chemical properties

Experimental and calculated electronic spectra for two enantiomers and safinamide salt in aqueous solution are graphically presented in Fig. 5a, while the experimental ECD spectrum of mesylate salt together the calculated spectrum are shown in Fig. 5b. SMS exhibited the absorption maximum at 227 nm and three very weak bands between 260 and 280 nm. The maximum peak obtained from TD-DFT was 226 nm, which was assigned to $\pi \rightarrow \pi^*$ transitions due to the chromophores C=C, C=O and C=N bonds, according to NBO analysis (Table 2). A similar value was reported by Mali et al. for the UVVis spectrum of mesylate salt in methanolic solution [25]. Probably, the weak bands experimentally observed

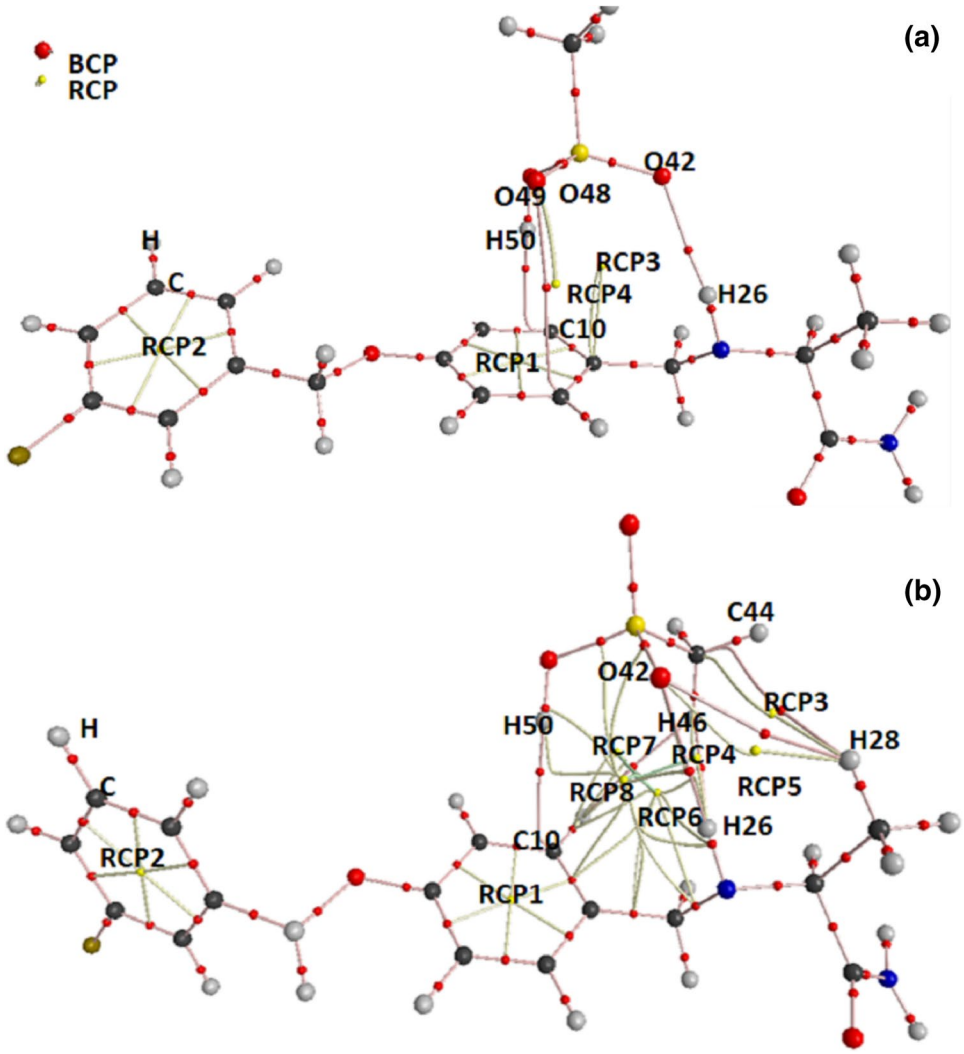

Fig. 4 Molecular graphic for SMS **a** in gas phase and **b** in aqueous solution calculated at B3LYP/6-31G* level of theory by using the AIM2000 program that shows the bond critical point (BCP) interactions and the ring critical point (RCP)

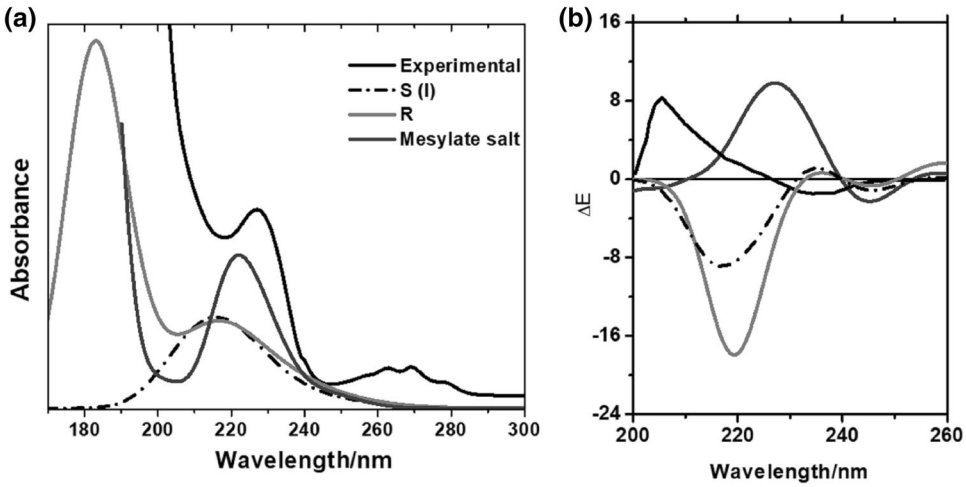

Fig. 5 Comparisons of experimental and calculated UV–Vis (**a**) and ECD (**b**) spectra of the two (*S*)- and (*R*)-enantiomers and safinamide mesylate salt in aqueous solution

between 260 and 280 nm could be attributed to $n \rightarrow \pi^*$ transitions, which were also predicted by NBO analysis in Table 2. Considering the measured absorbance spectra, we can also conclude that the predicted absorbance spectrum was found to be fully compatible with the experimental results.

The measured ECD spectrum of mesylate salt was consistent with the one calculated using the TDDFT method.

On the other hand, the experimental ECD spectrum of SMS in aqueous solution showed a strong correlation with the one predicted, as it was expected, while the predicted ECD spectra for two safinamide forms presented a negative Cotton effect, clearly evidencing their differences with the corresponding experimental results.

Highest occupied molecular orbital (HOMO) and lowest unoccupied molecular orbital (LUMO) are known as Frontier orbitals and the energy differences between two orbitals is recognized as energy gap [26]. Both gap and electronic distribution of two orbitals are important parameters to characterize the kinetic stability, chemical reactivity and spectroscopic properties [27]. As it can be seen in Fig. S1, the HOMO orbital is mainly located on the central aromatic rings having bonding characters, while LUMO orbitals are mainly located on the two rings in the enantiomer molecules but over the atoms between rings for SMS, indicating a high antibonding nature. Note that in SMS the HOMO orbital is symmetrically distributed on the central aromatic ring, with a contribution to N–H bond, which could explain its greater instability in solution.

We also calculated HOMO–LUMO energy gap (gap) using the B3LYP and CAM-B3LYP methods, which are listed in Table S6. The corresponding gap in water calculated by B3LYP method was found as 5.52 eV and 5.40 eV for the (*S*)-enantiomer and (*R*)-enantiomer, and the value for the SMS was equal to 5.57 eV; therefore, the gap for SMS was 0.07 wider than for the other species. As it can be seen, the energies gap calculated using CAM-B3LYP method, shows an increment in their values for all studied media. Those results are consistent with reports that indicate that DFT-B3LYP gives a more reasonable result for the optical band gap values than CAM-B3LYP functional [28].

The results showed a higher reactivity of the salt, especially in aqueous solution, while for the (*S*)-enantiomer, the gap energy increased slightly in solution. The gap and energy variations of the frontier orbitals together with the behaviours of the descriptors for the three species can be seen in Fig. S2. When SMS descriptors were analysed in depth, we observed low electronegativity and global hardness values but higher chemical potential and global softness values that indicate their tendency to react quickly and stabilize after interaction with nearby electronic charges [24]. The (*R*)-enantiomer showed the highest hardness value because it was the least reactive, while SMS was the most reactive and, for this reason, unstable. The lower electrophilicity and nucleophilicity indexes of the (*S*)-enantiomer could support its higher reactivity in relation to the (*R*)-enantiomer. As observed by Morales-Bayuelo et al. [29], the possibility of targeting either a catalytic active site (CAS) or a peripheral anionic site, MAO-B depends on the length of the bond. Taking into account that MAO-B inhibition is due to a retrodonation process on the central ring that is determined by steric and electronic effects [29], we think that the orientation of the propanamide group in the (*S*)-enantiomer is also an important factor for the activity of this molecule in biological media.

4.5 NMR and vibrational studies

The ^{1}H-NMR chemical shifts of (*R*)- and (*S*)-enantiomers and SMS were calculated at the B3LYP/6-31G* level of theory using the GIAO method [30]. The obtained results are listed in Table S7 and compared with experimental values reported by Leonetti et al. [24] and by Liang Zou [31], by means of the RMSD values. In general, the chemical shift differences between all molecules were not large, as shown by the corresponding RMSD values. Experimentally, the methyl protons appeared as a doublet at 1.59 ppm, while the theoretical chemical shift was predicted at around 1.87 ppm; for the mesylate salt the methyl signal was shifted upfield at 1.45 ppm. The most pronounced differences were observed in the methylene group, thus (*S*)-safinamide signals at 4.22 ppm and 5.19 ppm observed experimentally were assigned to methylene hydrogen at C6 and C14 respectively (H23-H24 and H34-H35 respectively); for SMS these signals appeared slightly displaced upfield (4.01 ppm and 5.16 ppm respectively). The theoretical chemical shifts predicted for the aromatic protons of both enantiomers and for the mesylate salt were in agreement with the experimental ones.

Both enantiomers and SMS were optimized with C_1 symmetries in the two media by using the B3LYP/6-31G* method. One hundred and forty-four normal vibration modes were expected for SMS, while 117 normal vibration modes were predicted for any of the enantiomers, all active in the IR and Raman spectra. The theoretical spectra, for all species, and experimental IR and Raman spectra of safinamide mesylate salt in solid state were also analysed in detail, as indicated in Figs. 6 and 7. The experimental spectra in the solid state and the predicted Raman spectra in gas phase for SMS showed a good correlation in Raman activities (see Fig. S3 and S4). The vibrational assignments for all species in aqueous solution were performed with the SQMFF procedure and taking into account that the scale that were used are those defined for the 6-31G* basis set. Table 3 shows the observed and calculated wavenumbers and assignments for all species in gas phase.

In the 4000–2700 cm^{-1} region, the infrared peaks from 3450 to 3200 cm^{-1} could be easily attributed to asymmetric and symmetric νN–H stretching modes, while the broad band observed in the infrared spectrum at around 3070 cm^{-1} can be assigned to the overlapping of νC–H stretching modes belonging to aromatic rings. Similarly, the experimental bands observed in the region below 3000 cm^{-1} can be assigned to the asymmetric and

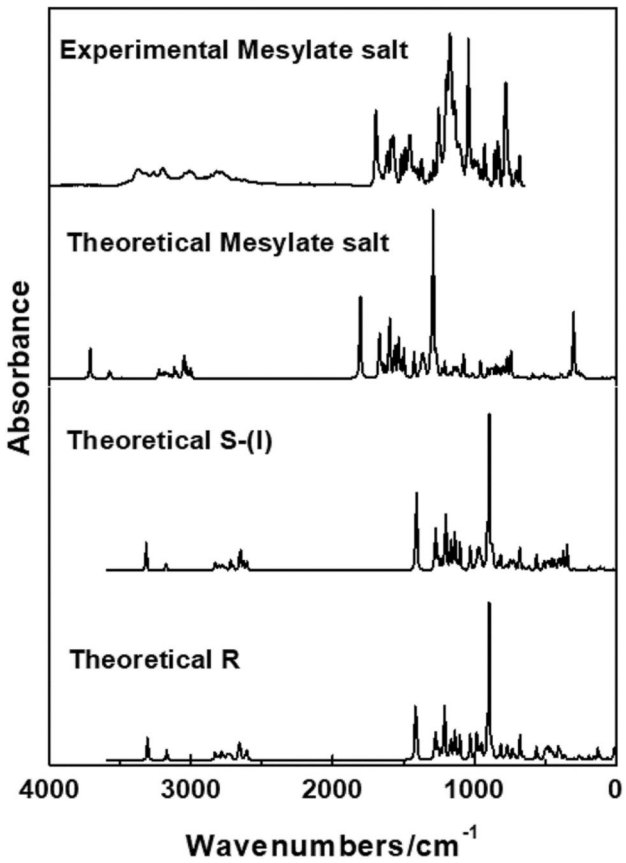

Fig. 6 Comparisons between the experimental FTIR spectrum of safinamide mesylate salt (SMS) in the solid state with the corresponding theoretical spectrum for (*S*)- and (*R*)-enantiomers, and the one predicted for the salt in gas phase at B3LYP/6-31G* level of theory

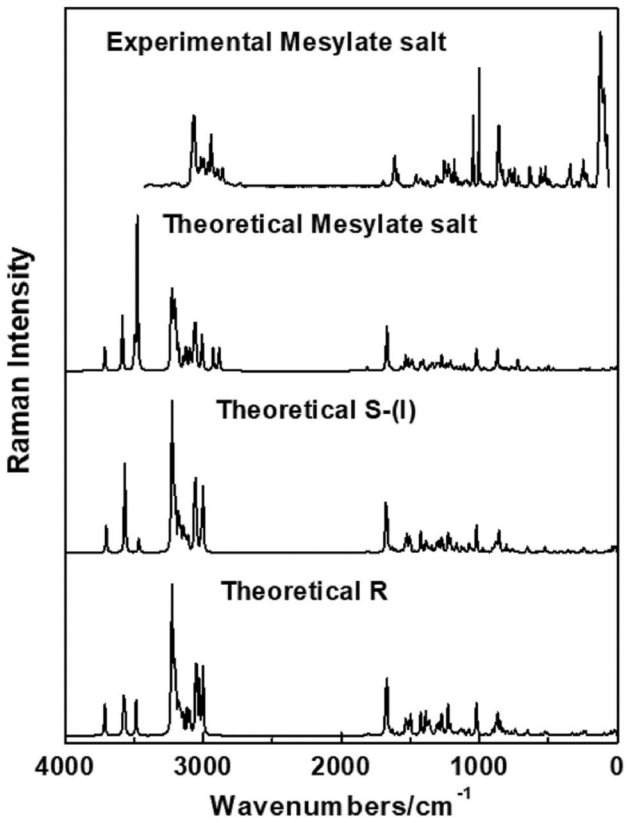

Fig. 7 Comparisons between the experimental Raman spectrum of safinamide mesylate salt (SMS) in the solid state with the theoretical one for its two (*S*)- and (*R*)-enantiomers, and the one predicted for the salt in gas phase at B3LYP/6-31G* level of theory

symmetric νCH_3 and νCH_2 stretching modes, as indicated in Table 3. The ring C–H stretching bands exhibited intense band in both experimental and theoretical Raman spectra. The two bands at 3019 cm^{-1} and 2943 cm^{-1} in Raman spectra which correspond at 3013 cm^{-1} and 2940 cm^{-1} in IR spectra involves the asymmetric $\nu_a CH_3$ and $\nu_a CH_2$ modes for all molecules. The Raman bands at 2966 cm^{-1}, 2927 cm^{-1} and 2897 cm^{-1} are assigned to symmetric $\nu_a CH_3$ and $\nu_a CH_2$ modes for all molecules. Those vibrations appear as shoulder in IR spectra. Note that the theoretical calculations overestimated the position of these bands with respect to the experimental results, for this reason theoretical frequencies were scaled by SQMFF methodology to obtain better agreement with the experiment.

In the 1700–1000 cm^{-1} region, in-plane deformation, wagging, rocking modes corresponding to the N–H, NH_2, CH_3, CH_2, and CH groups are expected. Thus, the strong band located in the infrared spectra at 1689 cm^{-1} was clearly assigned to νC=O stretching modes of three species although these modes for (*R*)- and (*S*)-enantiomeric forms were predicted by calculation at 1740 cm^{-1}. In agreement with predicted frequencies, the IR bands located from 1628 to 1584 cm^{-1} which were observed at 1616 cm^{-1}, 1612 cm^{-1} and 1590 cm^{-1} in Raman spectrum could be easily attributed to the νC=C and νC–C stretching modes of aromatic rings. The band of medium intensity observed at 1674 cm^{-1} was attributed to bending δNH_2. The calculations predicted the βC–H and βN–H in-plane deformation modes between 1515 and 1491 cm^{-1}, thus, the bands of medium intensity observed in experimental IR spectrum at 1515 to 1491 cm^{-1} and 1511 cm^{-1} and 1490 cm^{-1} in Raman spectrum were clearly assigned to these vibration modes. The symmetric and antisymmetric deformations, wagging, and rocking modes for CH_3 and CH_2 groups were attributed to the IR and Raman bands between 1472 and 1223 cm^{-1} because they were predicted by SQM calculations in this region [19]. The two $\nu_a SO_3$ stretching modes expected for the mesylate salt were attributed to the Raman band located at 1276 cm^{-1}, as it was predicted by calculation at 1283 cm^{-1}, while the remaining mode was attributed to the Raman band at 1093 cm^{-1}. The strong band observed at 1254 cm^{-1} in IR spectrum and 1255 cm^{-1}

Table 3 Observed and calculated wavenumbers (cm^{-1}) and assignments for both enantiomers of safinamide and its mesylate salt

Experimental[a]		B3LYP/6-31G* method[a]					
		Safinamide mesylate		Safinamide			
IR solid	Raman solid			*S*-(I)		R	
		SQM[b]	Assignments[b]	SQM[b]	Assignments[b]	SQM[b]	Assignments[b]
3447 sh	–	3558	ν_aNH_2	3559	ν_aNH_2	3549	ν_aNH_2
3377 m	3383sh	3438	ν_sNH_2	3425	ν_sNH_2	3419	ν_sNH_2
3330 m	3333sh	3353	ν(N4–H26)				
3263 m	3267sh	3334	ν(O42–H50)	3343	ν(N4–H26)	3323	ν(N4–H26)
–	3174 m	3100	ν(C22–H41)				
–	–	3096	ν(C14–H33)	3095	ν(C13–H32)	3094	ν(C13–H32)
–	–	3091	ν(C13–H32)	3095	ν(C19–H37)	3094	ν(C22–H41)
–	3085(15)	3085	ν(C21–H40)	3091	ν(C22–H41)	3090	ν(C19–H37)
–	–	3079	ν(C11–H31)	3080	ν(C14–H33)	3082	ν(C14–H33)
–	–	3075	ν(C19–H37)	3076	ν(C18–H36)	3077	ν(C18–H36)
3072 sh	3073(31)	3072	ν_aCH_3(C42)	3065	ν(C21–H40)	3066	ν(C21–H40)
	3066(31)	3065	ν(C10–H30)				
		3064	ν_aCH_3(C44)	3052	ν(C10–H30)		
3042 sh	3042(7)	3048	ν(C18–H36)			3048	ν(C10–H30)
	3031sh			3036	ν(C11–H31)	3036	ν(C11–H31)
3013 m	3019(12)	3012	ν_aCH_3(C9)	3018	ν_aCH_3	3017	ν_aCH_3
2997 sh	2998(12)	2995	ν_aCH_3(C9)	2987	ν_aCH_3	3001	ν_aCH_3
2980 sh	2966(11)	2968	ν_sCH_3(C42)	2970	ν_aCH_2(C6)	2983	ν_aCH_2(C6)
2940 m	2943(23)	2940	ν_aCH_2(C6)	2925	ν_sCH_2(C6)	2935	ν_sCH_3
	2927(8)	2930	ν_sCH_3(C9)	2924	ν_sCH_3	2928	ν_sCH_2(C6)
2897 w	2897(8)	2924	ν_aCH_2(C16)	2922	ν_aCH_2(C16)	2922	ν_aCH_2(C16)
2860 w	2859(8)	2883	ν_sCH_2(C16)	2902	ν(C7–H25)	2889	ν(C7–H25)
2818 m	2826 w	2806	ν_sCH_2(C6)	2878	ν_sCH_2(C16)	2878	ν_sCH_2(C16)
2786 m	–	2767	ν(C7–H25)				
1689 vs	1696(3)	1745	ν(C15–O3)	1740	ν(C15–O3)	1743	ν(C15–O3)
1628 sh	1616(13)	1619	ν(C10–C13)	1619	ν(C18–C20)	1619	ν(C10–C13)
1614 m	1612(13)	1613	ν(C18–C20)	1617	ν(C10–C13)	1618	ν(C18–C20)
1589 m	1590(6)	1600	ν(C20–C22), ν(C17–C19)	1600	ν(C20–C22)	1600	ν(C20–C22)
1584 sh		1578	ν(C8–C10), ν(C11–C8)	1579	ν(C11C8), ν(C12C14)	1580	ν(C13C12), ν(C11C8) ν(C8C10)
1574 m	1576 sh	1570	δNH_2				
1553 sh	–	1555	βC14–H33	1532	δNH_2	1540	δNH_2
1515 m	1511	1514	βC21–H40	1514	βC11H31	1515	βC11H31ν(C12C14)
1491 m	1490sh	1493	βC19–H37	1493	ν(C17C19)	1493	ν(C17C19)
		1468	δaCH_3(C9)	1484	βN5–H26	1490	βN5–H26
1472 sh	1475 sh	1467	δCH_2(C6)	1467	δCH_2(C16)	1469	δaCH_3
	1470 sh	1464	δCH_2(C16)	1462	δaCH_3	1468	δCH_2(C16)
1456 m	1457(5)	1455	$wagCH_2$(C16)	1456	δaCH_3	1461	δaCH_3
	1446sh	1453	δaCH_3(C9)	1455	ν(C17C18)	1455	ν(C17C18)
	1434 sh	1425	δaCH_3(C44)	1442	δCH_2(C6)	1441	δCH_2(C6)
1425 vw	1425(4)	1425	$wagCH_2$(C6)	1425	ν(C14–C11)	1425	ν(C14–C11)
1417 sh	1420(3)	1420	δaCH_3(C44)				
1402 w	1402sh	1397	$wagCH_2$(C16)	1398	$wagCH_2$(C16)	1398	$wagCH_2$(C16)
1373 m	1379(3)	1394	ρ'C7–H25, $wagCH_2$(C6)		$wagCH_2$(C6)	1370	$wagCH_2$(C6)
	1371sh	1379	βC14–H33	1363	δsCH_3	1359	δsCH_3
		1364	δsCH_3(C9)	1341	ρCH_2(C6)	1342	ρC7H25
1328 vw	1327sh	1328	δsCH_3(C44)	1333	ρC7H25	1334	ν(C15–N5)

Table 3 (continued)

Experimental[a]		B3LYP/6-31G* method[a]					
		Safinamide mesylate		Safinamide			
IR solid	Raman solid			*S*-(I)		R	
		SQM[b]	Assignments[b]	SQM[b]	Assignments[b]	SQM[b]	Assignments[b]
	1322sh	1320	ρC7–H25, βC14–H33	1323	ρ′C7H25, ν(C15–N5)	1322	βC14H33
		1316	ν(C17–C18)	1316	ν(C21C22), ν(C19C21)	1316	ν(C21–C22)
1311 w	1309(5)	1307	ρC7–H25	1313	βC11H31, βC10H30	1311	ρ′C7H25
		1301	ν(C13–C12)	1306	ν(C8–C10)	1307	ρ′C7H25, ν(C13–C12)
1290 w	1288(3)	1283	βC18–H36	1284	βC21H40, ρCH_2(C16)	1284	βC21H40, ρCH_2(C16)
1275 sh	1276(3)	1282	$\nu_a SO_3$				
1254 s	1255(12)	1265	ν(C20–F1)	1265	ν(C20–F1)	1266	ν(C20–F1)
		1264	ν(C21–C22)	1251	ν(C12–O2)	1251	ν(C12–O2)
	1248(8)	1251	ν(C12–O2)	1234	ρCH_2(C16)	1232	ρCH_2(C16)
1237 sh	1239(6)	1235	ρCH_2(C6)	1231	ρCH_2(C16)	1230	ρCH_2(C6)
1223 vw	1223(10)	1222	ρCH_2(C16)				
	1214(7)	1205	ν(C14–C11)				
1195 s	1196sh	1198	ν(C8–C6)	1189	ν(C8–C6)	1186	ν(C8–C6)
1173 vs	1183(12)	1174	ν(N4–C7)	1176	βC10H30, βC13H32	1175	βC10H30, βC13H32
	1166(4)	1171	βC13–H32			1162	βC21H40, βC19H37
	1161(5)	1161	βC22–H41	1161	βC21H40, βC19H37		
1139 w	1139sh	1140	βC11H31, ν(C17–C16)	1141	βC18H36, ν(C17–C16)	1141	βC18H36, ν(C17–C16)
1115 w	1116sh	1130	ν(N4–C6)	1130	ρCH_3	1126	ν(N4–C7), ρCH_3
1105 w	1104 sh	1106	βC10H30, ν(C19–C21)	1108	βC14H33ν(N4–C7)	1117	βC14H33
1095 sh	1093(3)	1101	$\nu_a SO_3$	1101	ρ′CH_3	1099	ρNH_2, ρ′CH_3
1078 w	1077sh	1083	ν(C7–C9)	1088	ρNH_2	1078	ν(C7–C9), τN4–H26
		1075	βC10H30, ν(C19–C21)	1076	βC22H41	1075	βC22H41, ν(C19–C21)
1060 sh	1060sh	1056	βN5–H26, ν(N4–C7)	1047	ν(N4–C6)	1040	ν(N4–C6)
1041 vs	1044(31)	1038	ν(C16–O2)	1039	ν(C16–O2)	1037	ν(C16–O2)
		1011	β$R_1(A_1)$, ν(C12–C14)	1011	β$R_1(A_1)$	1028	δ(C6N4C7)
1001 w	1003(51)	1001	β$R_1(A_2)$	1001	β$R_1(A_2)$	1010	β$R_1(A_1)$
994 w	991(4)	999	ρNH_2, ρCH_3(C9)				
		989	ρ′CH_3(C44)	990	ν(C7–C9)	1001	β$R_1(A_2)$
977 w	978sh	981					
		980	ρCH_3(C42)				
		971	γC21–H40	970	γC21H40	970	γC19H37
	966 h	968	γC10–H30, γC11–H31	961	τwCH_2(C16)	962	τwCH_2(C16)
954 w	953sh	959	τwCH_2(C16), γC11–H31	956	τwCH_2(C6)	950	γC11H31
943 sh	948sh	943	γC10–H30	949	γC11H31		
928 m	926sh	920	τwCH_2(C16), ν(C12–C14)	942	γC10H30	937	γC10H30
				920	τwCH_2(C16), ν(C17–C16)	919	τwCH_2(C16), ν(C17–C16)
908 sh	909 sh	902	τwCH_2(C6)			908	ν(C7–C9), τwCH_2(C6)
896 w	897sh	893	γC19–H37	894	γC22H41	894	γC22H41, γC19H37
872 w	863(23)	865	γC18–H36	865	γC18H36	866	γC18H36
857 m	859(27)	847	ν(C12–C14)	857	γC14H33, τwCH_2(C6)	858	γC14H33
834 m	831(7)	845	γC11–H31	845	ν(C13–C12)	847	γC18H36
825 m		831	γC13–H32	831	γC14H33	834	γC14H33
			ρ′CH_3(C42)	816	γC13H32	818	γC13H32
801 w	802sh	802	γC14–H33	807	γC13H32	804	γC13H32, γC10H30
		794					
	786(7)	784	γC22–H41	787	γC19H37	786	γC22H41, γC21H40

Table 3 (continued)

Experimental[a]		B3LYP/6-31G* method[a]					
		Safinamide mesylate		Safinamide			
IR solid	Raman solid			*S*-(I)		R	
		SQM[b]	Assignments[b]	SQM[b]	Assignments[b]	SQM[b]	Assignments[b]
778 vs	777(8)	776	ν_sSO_3	776	ν(C7–C15)	780	ν(C7–C15)
	750(4)	752		749	$\tau R_2(A_1)$	762	τN4–H26
745 w	746(8)	743	γC15=O3	736	γC15=O3	740	γC15=O3
721 sh	718(5)	725	ν(C7–C15)			731	τN4–H26, $\tau R_2(A_1)$
704 w	704sh	697	$\tau R_2(A_1)$, $\tau R_3(A_2)$	711	$\tau R_2(A_1)$	710	$\tau R_2(A_1)$
680 m		695	ν(C44–S43), ν_sSO_3	698	$\tau R_2(A_1)$		
		674	$\tau R_3(A_2)$, $\beta R_1(A_1)$	672	$\tau R_3(A_2)$	673	$\tau R_3(A_2)$
	650sh	652	$\tau R_1(A_2)$	647	$\beta R_2(A_1)$, $\beta R_3(A_1)$	648	$\beta R_2(A_1)$, $\beta R_3(A_1)$
	636(8)	644	$\beta R_1(A_1)$	635	$\beta R_3(A_2)$	636	$\beta R_3(A_2)$
	630sh	630	$\beta R_3(A_2)$, δ(N4C6C8)	617	τwNH_2	603	τwNH_2
	580sh	561	γC20–F1, $\beta R_2(A_1)$	577	$\tau R_2(A_1)$	573	τwNH_2
	555(8)	555	γC20–F1, γC17–C16	558	γC20F1, γC17C16	558	γC20F1, γC17C16
	536(4)	526	τNH_2	542	δ(N4C7C15)	544	ρC15=O3
	521(9)	519	$\beta R_2(A_2)$, τNH_2	520	$\beta R_2(A_2)$	520	$\beta R_2(A_2)$
	510 sh	515	ρC15=O3, δ(C6N4C7)			515	δ(C9C7N4)
		498	βC12–O2	504	γC12O2	498	γC12O2
	493(3)	493	δ_sSO_3, $\beta R_2(A_2)$	496	ρC15=O3		
	482sh	485	βC17–C16	488	βC12O2	487	βC12O2, δ(C12O2C16)
		457	δ_aSO_3, δ_sSO_3	475	δ(C9C7N4), δ(C6N4C7)	450	$\tau R_2(A_1)$, $\tau R_2(A_2)$
		449	δ_aSO_3, δ_sSO_3				
	444sh	441	$\tau R_2(A_2)$, $\tau R_3(A_2)$	441	$\tau R_2(A_2)$	440	$\tau R_2(A_2)$
	426sh	428	δ(C7C15N5)	417	βC20–F1	417	βC20–F1
	419sh	420	βC20–F1,	411	$\tau R_1(A_1)$		
	408sh	412	$\tau R_2(A_1)$, $\tau R_2(A_2)$			409	$\tau R_1(A_1)$
	350(6)	352	δ(N4C7C15), $\tau R_2(A_1)$	379	$\tau R_2(A_1)$	396	δ(C7C15N5)
	342(11)	334	δ_aSO_3			356	$wagNH_2$
		325	δ_sSO_3	328	βC8C6	350	βC8C6
	313sh	323	βC8–C6	323	δ(C7C15N5), γC8C6	315	$\tau R_2(A_1)$, γC8C6
	292(4)	306	τS43–O49–H26–N4	296	$wagNH_2$		
		276	δ(C9C7C15)			275	δ(C9C7C15)
	260(8)	268	$\rho'SO_3$	263	δ(C9C7C15)	260	βC17C16
	247(15)	247	βC12–C16	256	βC17C16		
		236	$\tau R_3(A_2)$,	241	τN4–C7, δ(C9C7C15)	238	$\tau R_3(A_2)$
	227(10)	232	δ(C9C7N4)	236	$\tau R_3(A_2)$	232	$\tau R_3(A_2)$
		216	τN4–H26, τwNH_2	222	$\tau R_2(A_2)$		
		210	τwCH_3(C9)	218	τwCH_3	214	τwCH_3
	197(6)	198	τS43–O49–H26–N4				
		186	τwSO_3,τwCH_3(C44)				
	176(9)	166	$\tau R_2(A_1)$, τwNH_2	167	δ(C12O2C16)	168	δ(N4C6C8)
		150	δ(S46O49Na50)	147	τN4–C7 $\tau R_2(A_1)$	154	τN4–H26
	122(100)	117	τN4–C7	114	τN4–C7τN4–H26	128	τN4–C7
	97(90)	96	δ(C9C7C15)				
	75(82)	76	ν(O49–H26)	83	τwC12O2	81	τwC12O2
		67	τN4–C7				
		61	τN4–H26	61	τC7–C15 $wagNH_2$	62	δ(O2C16C17)
		50	τN4–H26, τN4–C7	50	τN4–C7	59	τC7–C15

Table 3 (continued)

Experimental[a]		B3LYP/6-31G* method[a]					
		Safinamide mesylate		Safinamide			
IR solid	Raman solid			*S*-(I)		R	
		SQM[b]	Assignments[b]	SQM[b]	Assignments[b]	SQM[b]	Assignments[b]
		46	τN4–C7, τN4–H26				
		41	δ(S43O49H26)	44	τC7–C15	38	τN4–C6
		38	δ(O2C16C17), γC8–C6				
		34	τN4–H26, τN4–C7	30	τN4–C6	36	τN4–H26, τN4–C7
		26	τS46–O49, τN4–C7				
		21	δ(O49H26N4)	20	τN4–H26	20	τN4–H26
		15	τN4–C6	17	τO2–C16	15	τO2–C16
		13	τwC16O2	12	τwC16O2	11	τwC8C6, τwC16O2
		9	τO2–C16, τwC12O2				

ν, stretching; β, in-plane deformation; γ, out-of-plane deformation; wag, wagging; τ, torsion; β_R, deformation ring τ_R, torsion ring; ρ, rocking; τw, twisting; δ, deformation; a, antisymmetric; s, symmetric; (A_1), Ring1; (A_2), Ring2

[a]This work

[b]From scaled quantum mechanics force field

in Raman spectrum was assigned to the ν(C–F) stretching modes as it was predicted by calculations. The associated vibrational modes, including C–N and C–C vibrations, according to the calculated results, were attributed to 1214 cm^{-1} and 1196 cm^{-1} in Raman spectrum by ν(C–C) stretching modes and 1173 cm^{-1} and 1115 cm^{-1} in IR spectrum by ν(C–N) stretching modes. The very strong band at 1041 cm^{-1} in IR spectrum observed at 1044 cm^{-1} in Raman spectrum was assigned to ν(C–O) stretching mode.

For the 1000–10 cm^{-1} region, the N–H, NH_2, CH_3, CH_2, and CH group torsion and twisting modes, and the deformation (β_R) and torsion (τ_R) modes corresponding to the two rings were assigned taking into account the calculations and the assignments for similar compounds [32, 33], as it can be seen in Table 3.

4.6 Force Field analysis

The force constants for the (*S*)- and (*R*)-enantiomer of safinamide and SMS were calculated from their corresponding force fields expressed in Cartesian coordinates and were then transformed to normal internal coordinates using the MOLVIB program [20], as it is presented in Table S8 where they are compared with those reported for potassium borosulphate salts [34]. The *f(νC=O), f(νCH$_2$),* and *f(νCH$_3$)* constants for the (*S*) form were slightly lower than those corresponding to the (*R*) form. This variation can be perfectly justified because those three C=O, CH_2, and CH_3 groups belong to alaninamide, which is the most reactive group in the (*S*) form, as it was revealed by MEP studies and gap energies. In general, for all species the values decreased in solution with some exceptions, for instance, in the *f(νC-H), f(νCH$_2$),* and *f(νCH$_3$)* constants. Note that the *f(νC=O)* constants notably decreased in all species in solution, as it is expected, because these regions clearly are sites of H bond formation. Lower values for *f(νNH$_2$)* constants of salt were calculated, which can be easily attributed to its higher capability of H bond formation and the higher reactivity due to its ionic nature, as supported by the AIM and gap energy studies. When the *f(νS=O)* force constants for the mesylate salt in both media were compared with those reported for borosulphate, we observed higher values in these two compounds because both salts have SO_4 instead of SO_3 groups, like the mesylate salt. Here, the higher values in the *f(νS=O)* and *f(δO=S=O)* constants observed for borosulphate were attributed to the presence of a higher number of sulphate groups in this salt than in mesylate salts.

4.7 MAO-B inhibitor properties and NBO analysis

In this paper we will describe just one of the structures; we evaluated the energetic stability and nature of (*S*)-safinamide interactions in MAO-B binding site. Our results showed that (*S*)-safinamide binds non-covalently to the enzyme in front of the flavin adenine dinucleotide (FAD) cofactor in the active site, as shown in Fig. 8. The analysis revealed that the amine group was directed towards the flavin group of FAD, while the fluorobenzene ring was directed away from the site. In addition, the carbonyl group of safinamide was directed towards hydrophobic residues of Tyr60, Phe343, and Tyr398, and the

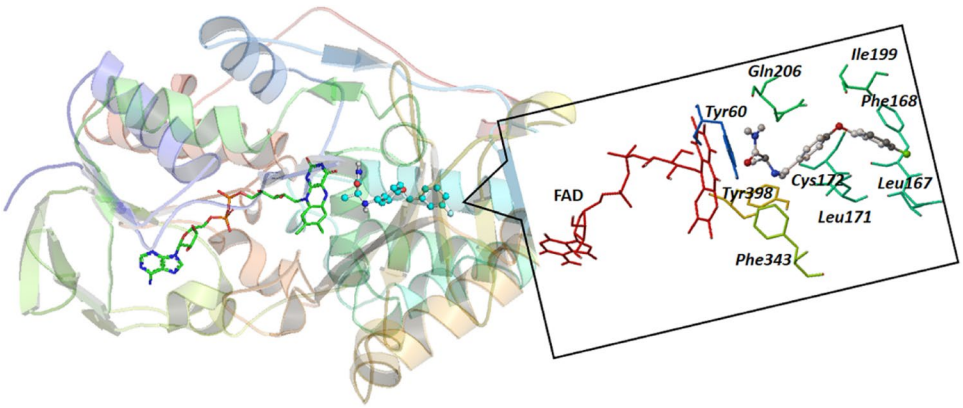

Fig. 8 Active site of MAO-B-(*S*)-safinamide. The FAD cofactor and safinamide are green-stick and cyan ball-and-stick representation, respectively. On the right, the residues of binding pocket are shown as sticks, and safinamide is presented in ball-and-stick style in grey colour

fluorobenzene ring interacting with Ile199, Phe168, and Leu167 hydrophobic residues, too. The analysis confirmed that safinamide interacted with MAO-B in the hydrophobic active site, a structural requirement for inhibiting the enzyme [11].

The binding energy of the most thermodynamically stable conformation was found to be − 8.8 kcal mol^{-1} with an inhibition constant of 0.35 μM. The last value was near to K_i of 0.5 μM reported for safinamide bound to human MAO-B [24]. The binding site interaction was investigated by NBO calculation. The residues in the binding cavity induced an electric charge rearrangement on the safinamide molecule, with a decrease in all atomic charges. The main donor–acceptor energy interaction energies resulting from NBO calculations are given in Table 4. The interaction energies of safinamide with Tyr60 residue were estimated within 3–8 kJ mol^{-1} from two lone pairs of the oxygen atom of C=O group to C-H Tyr60. The distance predicted by this interaction is 2.0 Å, as it is shown in Fig. S5. Another important electronic delocalization contribution was observed by interaction with Leu167 residue, confirming the hydrophobic interaction at that site. A similar kind

Table 4 Main delocalization energy (in kJ/mol) for the binding site of safinamide with MAO-B at B3LYP/6-31G* level of theory

Delocalization			
Tyr60-→NH_2 (safinamide)		**Safinamide→Tyr60**	
*σC5–H152→σ*N323–H314*	8.23	*LP (1) O318→σ*C7–H153*	15.75
		*LP (2) O318→σ*C7–H153*	30.85
Leu167→C–H (fluorobenzene ring of safinamide)		**Safinamide→Leu167**	
*σC22–H180→σ*C308–H339*	29.88	*σC308–H338→σ*C22–H180*	26.63
Phe168→NH_2 (safinamide)		**Safinamide→Phe168**	
*σC27–H175→σ*C308–H339*	1.45	*σC308–H339→σ*C22–H180*	6.37
*σC27–H175→σ*C316–H334*	19.98	*σC308–H339→σ*C27–H175*	18.35
*σC29–H177→σ*C316–H334*	5.81	*σC316–H334→σ*C27–H175*	7.61
		*πC304–C308→σ*C27–H175*	8.40
Cys172→C–H (middle ring of safinamide)		**Safinamide→Cys172**	
*σC41–H198→σ*C305–H332*	8.27	*πC299–C300→σ*C39–H189*	6.19
*LP O35→σ*C301–H333*	6.23	*πC301–C305→σ*C37–H184*	36.41
		*σC305–H332→σ*C41–H198*	8.40
Gln206→NH_2 (safinamide)		**Safinamide→Ile199**	
*LP O67→σ*N323–H313*	12.37	*σC316–H334→σ*C58–H218*	10.66
Phe343→NH_2 (safinamide)		**Safinamide→Phe343**	
*πC74–C76→σ*C320–H329*	5.35	*σC320–H328→σ*C76–H237*	5.98
*σC76–H237→σ*C320–H329*	8.40	*σC320–H329→σ*C76–H237*	7.69
Tyr398-→NH (safinamide)			
*πC95–C96→σ*N311–H321*	10.41		
*σO97–H262→σ*N311–H321*	8.36		
*LP (2) O97→σ*N311–H321*	7.56		

Main delocalization energies from MAO-B residues to safinamide expressed in bold letters

of interaction was predicted for Phe168 and Cys172 residues. A strong interaction from the lone pair of O atom to safinamide with a distance of 2.0 Å also contributed to Cys172–safinamide interaction. Finally, strong interactions were predicted from Tyr398 to N–H group of safinamide with a distance of 2.2 Å. Those results show the importance of carbonyl and amine groups of safinamide as MAO-B inhibitors [11].

5 Conclusions

The electronic spectrum, structural and electronic features of the antiepileptic and antiparkinsonian drug safinamide in two (*S*) and (*R*) enantiomer forms and their (*S*)-safinamide mesylate salt were examined using DFT method. Our results showed that the geometries of the molecules are optimized in the C1 configuration and the calculated geometry is in good agreement with experimental data. The theoretical charge density distribution, in gas phase and aqueous solution, indicated the (*S*)-enantiomer corresponds to the *S*-(I) polymorphic form experimentally observed. Depending on the total energy, the (*S*)-enantiomer in aqueous solution is more stable than the other species. The experimental absorption bands were attributed to electronic transition in the calculated spectrum from $\pi \rightarrow \pi^*$, which contributed to the stability of molecules, and (*S*)-enantiomer and SMS evidenced a high contribution of $LP \rightarrow \pi^*$ interaction. Topological and NBO analysis revealed the strength and chemical bonding details of all molecules, as well as the presence of an intramolecular N–H hydrogen bonding interaction with higher contribution for (*S*)-enantiomer. The frontier orbitals, gap, absorption, NMR, IR, and Raman spectra were examined in detail. The studies of the frontier orbitals explain the greater reactivity of the salt, and the lower electrophilicity and nucleophilicity indexes of the (*S*)-enantiomer would support its greater reactivity and probably, its higher activity as MAO-B inhibitor. The complete assignments of vibration normal modes for the salt and its two enantiomers are reported, and they are in reasonable agreement with the corresponding experimental data. The electrostatic potential maps show a high electronegative region on the C=O group and electrophilic centres on the H atoms belonging to the NH_2 group. The theoretical charge density study clearly afforded satisfactory details of structural information and charge density distribution that are the necessary parameters to interpret the drug-receptor interactions between the safinamide molecule and monoamine oxidase enzyme. Finally, the importance of safinamide polar groups in MAO B inhibition was analysed by using NBO calculation.

Acknowledgements This work was supported with grants from CIUNT Project No 26/D207 (Consejo de Investigaciones, Universidad Nacional de Tucumán) and UNSE Project 23/C136. The authors would like to thank Prof Tom Sundius for his permission to use MOLVIB.

Compliance with ethical standards

Conflict of interest The authors declare that they have no conflict of interest.

Ethical standard This study complied with ethical standards.

References

1. Deeks ED (2015) Safinamide: first global approval. Drugs 75:705–711. https://doi.org/10.1007/s40265-015-0389-7
2. Stocchi F, Torti M (2016) Adjuvant therapies for Parkinson's disease: critical evaluation of safinamide. Drug Des Dev Ther 10:609–618. https://doi.org/10.2147/DDDT.S77749
3. Fariello RG (2007) Safinamide, neurotherapeutics. J Am Soc for Exp Neuro Ther 4:110–116. https://doi.org/10.1016/j.nurt.2006.11.011
4. Blair HA, Dhillon S (2017) Safinamide: a review in Parkinson's disease. CNS Drugs 31:169–176. https://doi.org/10.1007/s40263-017-0408-1
5. Kulisevsky J (2016) Safi-namide—a unique treatment targeting both dopaminergic and non-dopaminergic systems. Eur Neurol Rev 11:101–105. https://doi.org/10.17925/ENR.2016.11.02.101
6. Dézsi L, Vécsei L (2014) Safinamide for the treatment of Parkinson's disease. Drugs 23:729–742. https://doi.org/10.1517/13543784.2014.897694
7. Caccia C, Maj R, Calabresi M, Maestroni S, Faravelli L, Salvatti R, Fariello RG (2006) Safinamide: from molecular targets to a new anti-Parkinson drug. Neurology 67:18–23. https://doi.org/10.1212/WNL.67.7_suppl_2.S18
8. Ravikumar K, Sridhar B (2010) Two polymorphs of safinamide, a selective and reversible inhibitor of monoamine oxidase B. Acta Cryst 66:317–320. https://doi.org/10.1107/S0108270110019384
9. Reddi A, Mujahid M, Sasikumar M, Muthukrishnan M (2014) A new enantioselective synthesis of the anti-parkinson agent safinamide. Synthesis 46:1751–1756. https://doi.org/10.1055/s-0033-1341104
10. Zou L, Sun L, Zhang H, Hui W, Zou Q, Zhu Z (2017) Identification, characterization, and quantification of impurities of safinamide mesilate: process-related impurities and degradation products. J AOAC Int 100:1029–1037. https://doi.org/10.5740/jaoacint.16-0218
11. Cheng K, Li S, Lv X, Tian Y, Kong H, Huang X, Duan Y, Han J, Xie Z, Liao C (2019) Design, synthesis and biological evaluation of novel human monoamine oxidase B inhibitors based on a fragment in an X-ray crystal structure. Bioorg Med Chem Lett 29:1012–1018. https://doi.org/10.1016/j.bmcl.2019.02.008
12. Dennington R, Keith T, Millam J (2019) GaussView, version 6.1.1. Semichem Inc., Shawnee Mission
13. Frisch MJ, Trucks GW, Schlegel HB, Scuseria GE, Robb MA, Cheeseman JR, Scalmani G, Barone V, Petersson GA, Nakatsuji H, Li XM (2019) Gaussian 16, revision C.01. Gaussian Inc., Wallingford
14. Tomasi JPJ (1994) Molecular interactions in solution: an overview of methods based on continous distributions of the solvent. Chem Rev 94:2027–2094. https://doi.org/10.1021/cr00031a013

15. Marenich CJT, Cramer DG (2009) Universal solvation model based on solute electron density and on a continuum model of the solvent defined by the bulk dielectric constant and atomic surface tensions. J Phys Chem B. https://doi.org/10.1021/jp810292n
16. Weinhold F, Glendening ED (2013) NBO 6.0: natural bond orbital analysis programs. J Comput Chem 34:1429–1437. https://doi.org/10.1002/jcc.23266
17. Biegler-Köning DJBF, Schönbohm J (2001) A program to analyze and visualize atoms in molecules. Comput Chem 22:545–559. https://doi.org/10.1002/1096-987X(20010415)22:5%3c545:AID-JCC1027%3e3.0.CO;2-Y
18. Chain F, Iramain MA, Grau A, Catalán CAN, Brandán SA (2017) Evaluation of the structural, electronic, topological and vibrational properties of *N*-(3,4-dimethoxybenzyl)-hexadecanamide isolated from Maca (*Lepidium meyenii*) using different spectroscopic techniques. J Mol Struct 1128:653–664. https://doi.org/10.1016/j.molstruc.2016.09.043
19. Rauhut G, Pulay P (1995) Transferable scaling factors for density functional derived vibrational force fields. J Phys Chem 99:3093–3099. https://doi.org/10.1021/j100010a019
20. Sundius T (2002) Scaling of ab initio force fields by MOLVIB. Vib Spectros 29:89–95. https://doi.org/10.1016/S0924-2031(01)00189-8
21. Morris GM, Huey R, Lindstrom W, Sanner MF, Belew RK, Goodsell DS, Olson AJ (2009) AutoDock4 and AutoDockTools4: automated docking with selective receptor flexibility. J Comput Chem 30:2785–2791. https://doi.org/10.1002/jcc.21256
22. Joy M, Mathew B, Sudarsanakumar C (2018) Structural features of safinamide: a combined hirshfeld surface analysis & quantum chemical treatment. Chem Data Collect 17:404–414. https://doi.org/10.1016/j.cdc.2018.10.009
23. Binda C, Wang J, Pisani L, Caccia C, Carotti A, Salvati P, Edmondson DE, Mattevi A (2007) Structures of human monoamine oxidase B complexes with selective noncovalent inhibitors: safinamide and coumarin analogs. J Med Chem 50:5848–5852. https://doi.org/10.1021/jm070677y
24. Leonetti F, Capaldi C, Pisani L, Nicolotti O, Muncipinto G, Stefanachi A, Cellamare S, Caccia C, Carotti A (2007) Solid-phase synthesis and insights into structure–activity relationships of safinamide analogues as potent and selective inhibitors of type B monoamine oxidase. J Med Chem 50:4909–4916. https://doi.org/10.1021/jm070725e
25. Redasani VK, Mali BJ, Surana SJ (2012) Development and validation of HPTLC method for estimation of safinamide mesylate in bulk and in tablet dosage form. ISRN Anal Chem 10:135208. https://doi.org/10.5402/2012/135208
26. Fleming I (2010) Frontier orbitals and organic chemical reactions. Oxford University Press, Oxford
27. Özer Z, Kılıç T, Çarıkç S, Azizoglu A (2019) Synthesis, structural characterization, spectroscopic properties, and theoretical investigation of siderol acetate. Russ J Phys Chem A 93:2703–2709. https://doi.org/10.1134/S0036024419130235
28. Kurban M, Gündüz B, Göktaş F (2019) Experimental and theoretical studies of the structural, electronic and optical properties of BCzVB organic material. Optik 182:611–617. https://doi.org/10.1016/j.ijleo.2019.01.080
29. Morales-bayuelo A, Baldiris R, Vivas-reyes R (2013) Scale alpha and beta of quantitative convergence and chemical reactivity analysis in dual cholinesterase/monoamine oxidase inhibitors for the Alzheimer disease treatment using density functional theory (DFT). J Theor Chem. https://doi.org/10.1155/2013/768185
30. Ditchfield R (1974) Self-consistent perturbation theory of diamagnetism. Mol Phys 27:89–807. https://doi.org/10.1080/00268977400100711
31. Zou L, Sun L, Zhang H, Hui W, Zou Q, Zhu Z (2017) Identification, characterization, and quantification of impurities of safinamide mesilate: process-related impurities and degradation products. J AOAC Intern 100:1029–1037. https://doi.org/10.5740/jaoacint.16-0218
32. Romani D, Tsuchiya S, Yotsu-Yamashita M, Brandan SA (2016) Spectroscopic and structural investigation on intermediates species structurally associated to the tricyclic bisguanidine compound and to the toxic agent, saxitoxin. J Mol Struct 1119:25–38. https://doi.org/10.1016/j.molstruc.2016.04.039
33. Brandan SA, Márquez MJ, Márquez MB (2015) A structural and spectroscopic study on benzisozaxole methane sulfonic acid sodium salt (BOSNa). In: Descriptors, structural and spectroscopic properties of heterocyclic derivatives of importance for the health and the environment, 1 edn., chapter 6. Nova Science Publishing Inc., pp 132–157. ISBN: 978-1-63482-708-9
34. Brandán SA, Höppe HA, Kazmierczak K, Romano E (2013) A structural and vibrational study on the first condensed borosulfate, K5[B(SO4)4] by using the FTIR-Raman and DFT calculations. J Mol Struct 1037:294–300. https://doi.org/10.1016/j.molstruc.2012.12.042